Revised Scaling of Optical Distortions Caused by Compressible, Subsonic Turbulent Boundary Layers

Donald J. Wittich, III[*]
University of Notre Dame, Notre Dame, IN, 46556

Stanislav Gordeyev[†]
University of Notre Dame, Notre Dame, IN, 46556

and

Eric Jumper[‡]
University of Notre Dame, Notre Dame, IN, 46556

New measurements of optical aberrations caused by a compressible subsonic turbulent boundary layer are presented. These new measurements are based on more-accurate Malley Probe measurements made possible by developing new wind-tunnel test sections that greatly reduced vibration corruption that imprints itself on the Malley Probe's small-aperture, probe-beam deflection-angles. These new measurements give more-accurate levels of optical distortions for laser propagation through boundary layers, lowering previously-obtained values by ~ 30%. Using a similarity analysis based on these new measurements, a rigorous approach of extracting boundary-layer-related optical information from partially corrupted spectra is proposed and demonstrated by applying it to previously-obtained, vibration-corrupted measurements. Optical spanwise and streamwise length scales for a boundary layer are also presented and these statistical data is used to develop a method of creating realizations of 2-D wavefronts.

I.   Introduction

Aero-optics is the study of the wavefront aberrations that occur when an otherwise collimated laser beam, is passed through a variable-index-of-refraction turbulent flows. More specifically, aero-optics is concerned with compressible, subsonic or supersonic flows near the exit aperture of a beam, and is thus separate from the study of atmosphere propagation[1]. In practice, two canonical flows are of particular interest; the separated shear-layer, and the turbulent boundary layer.

Investigations of the optical characteristics of turbulent boundary layers date back to the early 1950's. Jumper and Fitzgerald [2] provided an excellent review of the most important results up through the 1990's. Despite this extensive amount of work, the aero-optics of turbulent boundary layers remains less understood than that of the separated shear layer, which has been studied extensively only since the 1990's. At least part of the reason for this is that the optical aberrations induced by a turbulent, weakly-compressible boundary layer are much less than those induced by a separated shear layer of similar Mach and Reynolds number. This means that the signal-to-noise ratio characteristic of most wavefront sensors can mask the optical characteristics in all but the thickest and highest-Mach-number subsonic turbulent boundary layers.

The exception to the signal-to-noise limitation of most wavefront sensor techniques is the Malley Probe based on a technique first reported by Malley et. al. in 1992 [3]. This instrument, whose details of operation are reported in [4,5], relies on the fact that aberrations on a laser beam's wavefront due to convecting flow structures in an aero-optic flow are themselves convecting. Further, based on Huygens's

---

[*] Graduate Research Assistant, Department of Aerospace and Mech. Eng., Student Member AIAA
[†] Research Assistant Professor, Department of Aerospace and Mech. Eng., Member AIAA
[‡] Professor, Department of Aerospace and Mech. Eng., Fellow AIAA

principle, a small-aperture laser probe beam propagated through the turbulent variable-index-of-refraction flow will emerge from the flow perpendicular to the wavefront of a larger beam propagated through the same flow. Measuring the deflection of the small-aperture probe beam as a function of time (jitter signal) records a time history of the slope of the wavefront as it passes by the probe beam. By knowing the convection velocity of the aberrating flow structures the slope of the wavefront in the streamwise direction can be converted into Optical Path Length (*OPL*) by integrating in time the product of the wavefront slope and the convection velocity. The Malley Probe signal is sufficiently sensitive to measure the small variations in wavefront imposed by weakly-compressible turbulent boundary layers; however, the Malley Probe beams also pick up vibrations and to the extent that the frequencies present in the vibration corruption overlap aero-optical frequencies, the deconvolution of OPL from the probe-beam's jitter signal can over estimate the *OPL*.

The Malley Probe relies on collecting jitter signals from two closely-spaced probe beams aligned in the streamwise direction to extract the convection velocity of the aberrating flow structures. The extraction of velocity as a function of disturbance frequency is described in Fig. 1. When the two jitter signals are correlated in the Fourier domain, phase plots of the phase delay between the two beams can be plotted as a function of frequency. Knowing the streamwise distance between probe beams, the slope of the phase plots gives a direct measure of the velocity as a function of frequency. As will be discussed later in this paper, these phase plots are also useful in identifying where vibration corruption is present and has been used in previous work in removing the vibration corruption from the calculation of *OPL* from Malley Probe jitter signals. This approach and has been extremely effective in measuring aero-optically-induced *OPL* for separated flows where any error due to small amounts of unremoved vibration corruption is an insignificant error to the relatively large *OPL*; however, as will be discussed in the paper, the *OPL* due to the turbulent boundary layer is sufficiently small that any unremoved vibration remaining in the jitter, especially at the lowest frequencies can introduce relevant error in deconvolved *OPL*.

For a fixed time delay, t, the phase shift for different periods is:

$$\phi_i = \frac{\tau}{T_i} 2\pi$$

The frequency for a given period is:

$$f_i = \frac{1}{T_i}$$
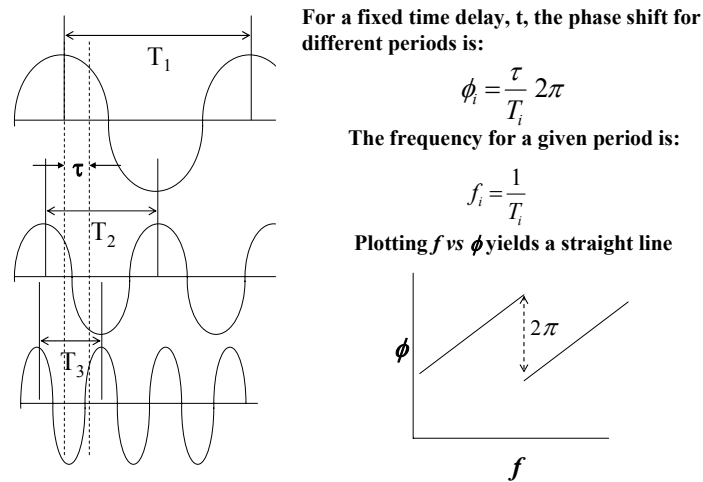
Plotting *f* vs *ϕ* yields a straight line

Figure 1. Malley Probe phase plots of convecting structures create lines (lower right-hand corner) which are used to extract convective velocity data.

The purpose of work presented in this paper is to specifically address this residual vibration error that has plagued the measurement of optical aberrations due to propagation through turbulent boundary layers in the past. This effort began by revisiting the design of the test section used in a previously-reported boundary-layer study[5]. The new design described below was successful in collecting the cleanest data yet recorded for the turbulent boundary layer. These data were further improved by using a more-powerful, 25 mW, HeNe laser in place of 5 mW laser of the earlier work. The higher-power laser provided an improved signal-to-noise ratio due to electrical noise that is not amplified as much due to being able to use less amplification. These new data were then used to construct a similarity method for making use of otherwise-vibration-corrupted jitter data to produce accurate measures of the optical character of turbulent boundary layers.

II.   Experimental Setup

The experiments reported here were conducted in a transonic, indraft wind tunnel in the Hessert Laboratory at the University of Notre Dame. The tunnel is driven by two Allis Chalmer 3,310 CFM vacuum pumps. The test section Mach number is controlled by adjusting a valve downstream of the diffuser.
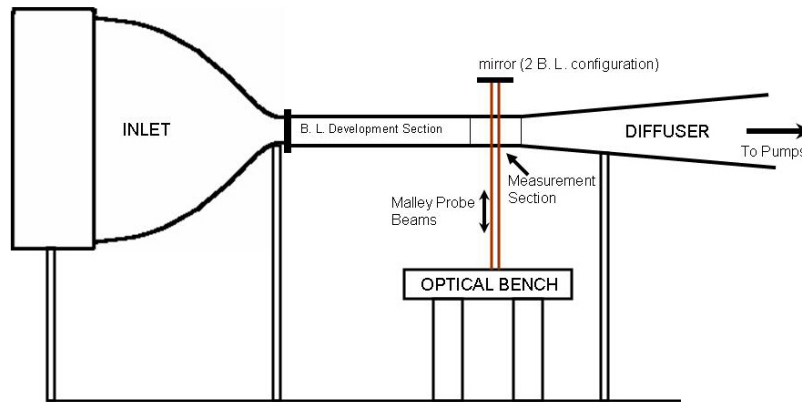

Figure 2: Wind Tunnel Schematic.

Two test sections were used in these experiments, composed of a common development length section and individual measurement sections, shown in Figure 2. All sections were rectangular and constructed primarily of Plexiglas, measuring 9.9 X 10.1 cm in a cross-section. To promote a turbulent development, the lower surface of the first 70.5 cm of development length was roughen with a grit paint compound that mimics the effect of medium grit sand paper. The upper surface is smooth for the entire length.

The single boundary layer measurement section was located immediately downstream of the development section. Five streamwise-arranged static pressure ports 2.54 cm apart and a single, total pressure port were mounted in the side wall of each test section, shown in Figure 3, left. The total pressure port was used only initially to determine that the total pressure loss inside the test section was negligible. After these initial determinations, the total pressure port was removed and the port covered.   The static ports were connected to a U-tube, mercury manometer and used to measure freestream Mach number.
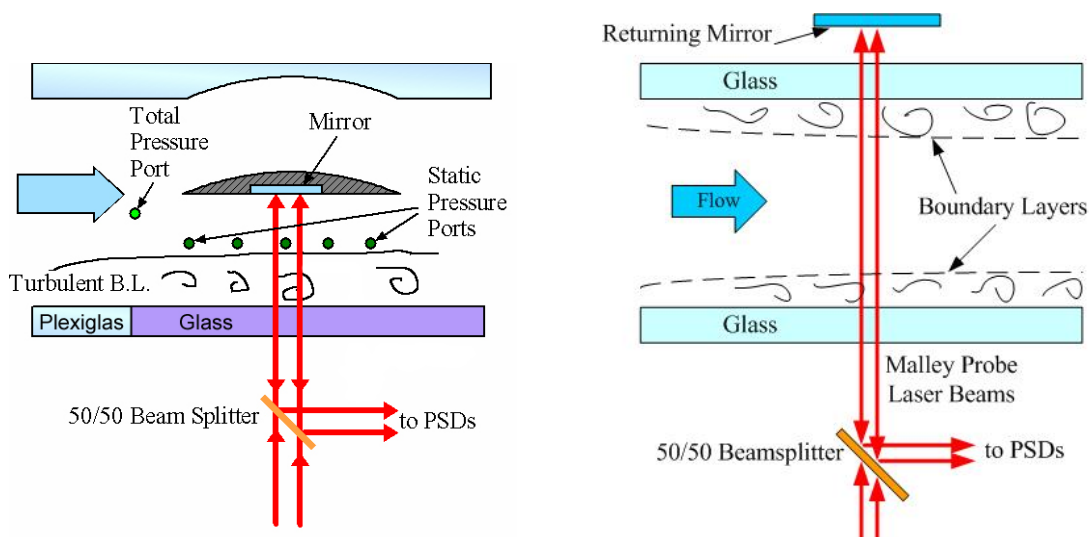

Figure 3: Left: Schematic of single boundary layer experiment measurement section; Right: Schematic of double boundary layer experiment measurement section.

The first measurement section was a modification of the test section described in [5]. The lower surface was replaced by plate glass to improve optical quality. The returning mirror and its mount were also replaced by bulkier components with the goal of reducing vibrations above 1 kHz. The mirror is 50 mm in diameter with a $\lambda / 10$ surface for the 633 nm laser used. The upper surface of the tunnel above the mirror is sculpted so as to prevent blockage effects of the mirror mount. Hotwire measurements were also acquired in this section at the same location as the Malley probe measurements.

Despite bulking up the mirror mount, the effects of vibration, though significantly reduced, were still present and corrupted the low-frequency end of the jitter signal spectrum. To accurately evaluate the spectral characteristics of the boundary layer, another measurement test section was constructed without a return mirror with plate glass on the upper and lower surfaces. In this section, the laser beams pass through the boundary layers on both the upper and lower surfaces so that they are unaffected by tunnel-induced vibrations, as shown in Fig. 3, right.

III.   Results

A. Hotwire Results.

The boundary layer profile along the bottom of the test section was measured with a single boundary-layer hotwire; the results are shown in Figure 4, left. Figure 4, right shows the same data in wall units. The freestream Mach number was 0.5. Using the Clauser method, the friction velocity, u_τ, was found to be 5.45 m/s. The profile in Figure 4, right, exhibits a clear log-law region from $y^+ \sim 700$ to 2400. The boundary layer displacement thickness, δ^*, was calculated as 2.86 mm and the momentum thickness, θ, was found to be 2.16 mm. The Reynolds number based on momentum thickness, $Re_\theta = U_\infty\theta/v$, was approximately 26,000 and the Reynolds number based on development length, $Re_x = U_\infty x/v$, was approximately 17.7 x 10^6, where x is the development length of 160 cm. The shape factor $H = \delta^*/\theta$ for this boundary layer was found to be 1.32, which agrees quite well with values for zero-pressure-gradient boundary layers[6] at this Re_θ.
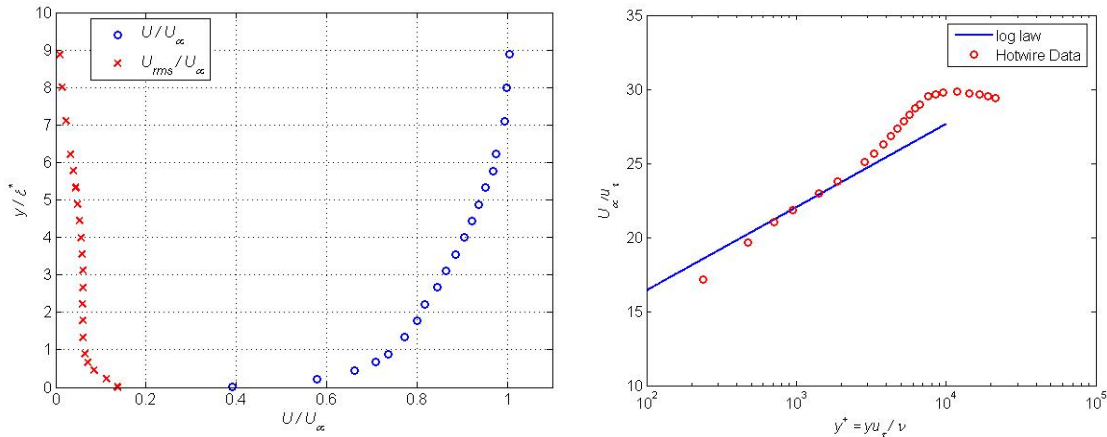

Figure 4: Left: Hotwire data of tunnel lower wall boundary layer profile; Right: Boundary layer profile in wall units. The solid line represents the log-law, $u^+ = (1/0.41) \, y^+ + 5.6$, the corresponding friction velocity, u_τ, is 5.45 m/s.

B. Malley Probe Results.

Figure 5a, shows the beam jitter power spectrum of a Malley Probe sample acquired at $M_\infty = 0.41$. Although vibration was reduced from that experienced in previous experiments[5], it still remained evident in the two large peaks at 1.5 and 2.4 kHz in Figure 5a. The corresponding phase data, shown in Figure 5b, shows a zero phase relationship between the two Malley probe beams at these frequencies, indicating vibration-related peaks. Electronic noise spikes are also evident at 5.8 kHz and at frequencies above 20 kHz.
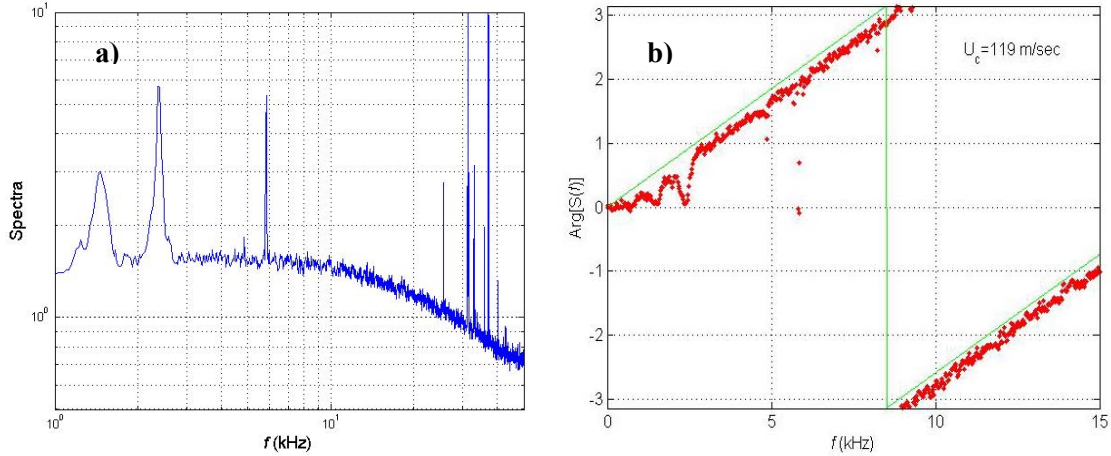
Figure 5: a) Malley Probe jitter power spectrum ($M_\infty = 0.41$); b) The corresponding Malley Probe phase data. The optical aberrations convect at $0.87U_\infty$.

From the phase data, the convective velocity, U_c was determined to be 119 m/s or $0.87U_\infty$. The shape of the spectrum in Figure 5a seemed to suggest that the power might be decreasing with frequency somewhere below 4 or 5 kHz, but the vibration peaks might be hiding any such roll off.

Another way to acquire information about the deflection angle spectrum is to remove the returning mirror and pass the laser beams through the entire test section, thus avoiding the spectrum contamination due to the mirror vibration, see Fig. 3, right. In this case, the beams pass through two independent boundary layers. The Malley Probe jitter power spectrum for beams passed through two boundary layers at Mach 0.41 is shown in Figure 6a, and its associated phase plot is shown in Figure 6b.
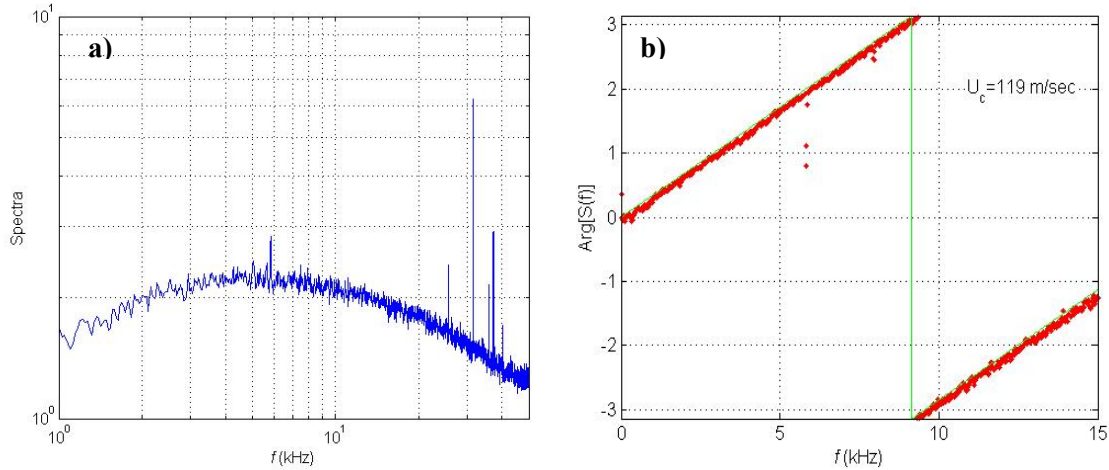

Figure 6: a) Jitter power spectrum for Malley probe beams through two boundary layers at $M = 0.41$; b) The phase plot. Optical aberrations convect at $0.87\ U_\infty$.

The most dramatic differences between Figure 5a and Figure 6a are that the large vibration peaks at 1.5 and 2.4 kHz are no longer evident and that the jitter quite clearly decreases with frequency below 5 kHz. Also, because the beams passed through two boundary layers, their optical signal was larger with respect to the electronic noise at 5.8 kHz. Thus, although it is still present, the effect of electronic noise has been reduced. In post-process, the jitter signals $\theta(t)$ were high-pass filtered at 1 kHz to remove the remaining effect of any low-frequency vibrations prior to computing *OPD* in the manner described by,

$$OPL(t) = -U_c \int \theta(t)dt$$
$$OPD(t) = OPL(t) - <OPL>$$

(1)

Because the two boundary layers are statistically independent, the OPD_{rms} for a single boundary layer was estimated as

$$OPD_{rms}^{Single\ BL} = \frac{1}{\sqrt{2}} OPD_{rms}^{Double\ BL}. \qquad (2)$$

The OPD_{rms} for samples collected at Mach numbers between 0.3 and 0.6 are shown in Figure 7 plotted against their associated scaling factor, $\delta^*\rho/\rho_{SL}M^2$, which was shown to be a correct scaling for subsonic compressible boundary layers[5]. The error bars account for electronic noise and any error in the beam separation width measurement. A linear fit through the data, also shown in Figure 7, gives the following revised scaling:

$$OPD_{rms} = (1.6 \pm 0.4) \times 10^{-5} \delta^* \frac{\rho}{\rho_{SL}} M^2. \qquad (3)$$

The previously obtained scaling[5] gave the value for the coefficient of 2.4×10^{-5}, thus overestimated the OPD_{rms} for boundary layers by approximately 30%. The reasons for this overestimation are discussed below.
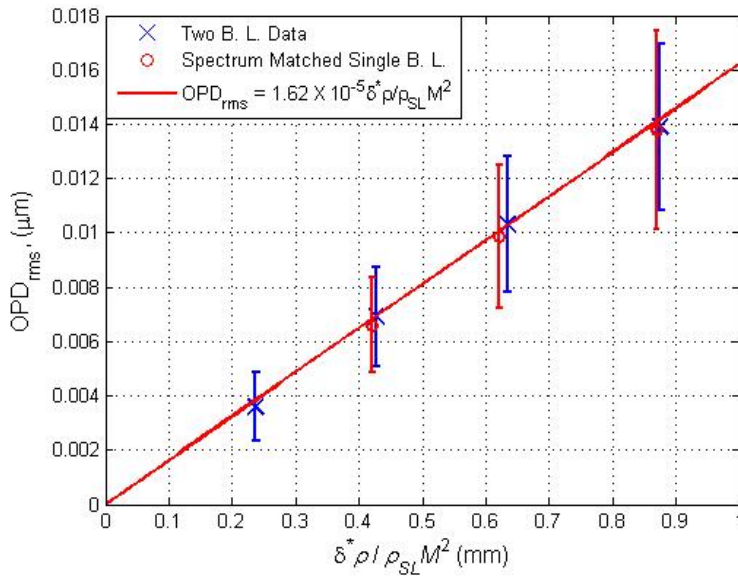

Figure 7: Boundary layer OPD_{rms} scaling.

C. Spectral Matching

Now we have a 'clean' boundary layer spectrum obtained from the two boundary layer experiment (Figure 6a), and the corresponding OPD obeys the scaling (density and Mach number) consistent with previous experiments. From (1) and (2) it follows the deflection angle scales as,

$$\theta \propto \frac{\rho/\rho_{SL}\delta^* M^2}{U_\infty}, \qquad (4)$$

where we have also noted that $U_c \sim U_\infty$. Thus, any linear function of the deflection angle, such as a Fourier transform, scales the same way. Thus, any boundary layer jitter spectrum can be presented as,

$$\hat{\theta}(f) = \frac{\rho}{\rho_{SL}} M^2 \frac{\delta^* f_{samp}}{U_\infty} \hat{\theta}_{norm}\left(f\delta^* / U_\infty\right), \tag{5}$$

where f_{samp} is the sampling frequency. The normalized jitter spectra, $\hat{\theta}_{norm}\left(St = f\delta^* / U_\infty\right)$, from the two boundary layer experiment are plotted in Figure 8, left, while the normalized spectra from the single boundary layer experiment are plotted in Figure 8, right. All spectra were normalized using a displacement thickness, δ^*. All spectra, except for M =0.32, collapse onto one curve, proving the scaling in (5) is indeed correct. This normalized spectrum exhibits a single peak at St ~ 0.1 and decay at both sides. The Mach 0.32 spectrum did not properly collapse in either experiment (not shown in Figure 7, right). It seems that the jitter signal is so weak at such a low Mach number, that results are often mixed. So, although the OPD_{rms} value fell in line with the others (Figure 7), this case is disregarded from here on. The normalized spectra have a slight power buildup (spectral aliasing) at high frequencies for the Mach 0.51 and 0.62 cases. This buildup suggests that the sampling frequency was possibly too low in these experiments. It should also be noted that if the Strouhal number of the abscissa is written in terms of the boundary layer thickness, δ, instead of the displacement thickness, the 'peak' of the boundary layer spectrum occurs near $St_\delta \sim 1$.
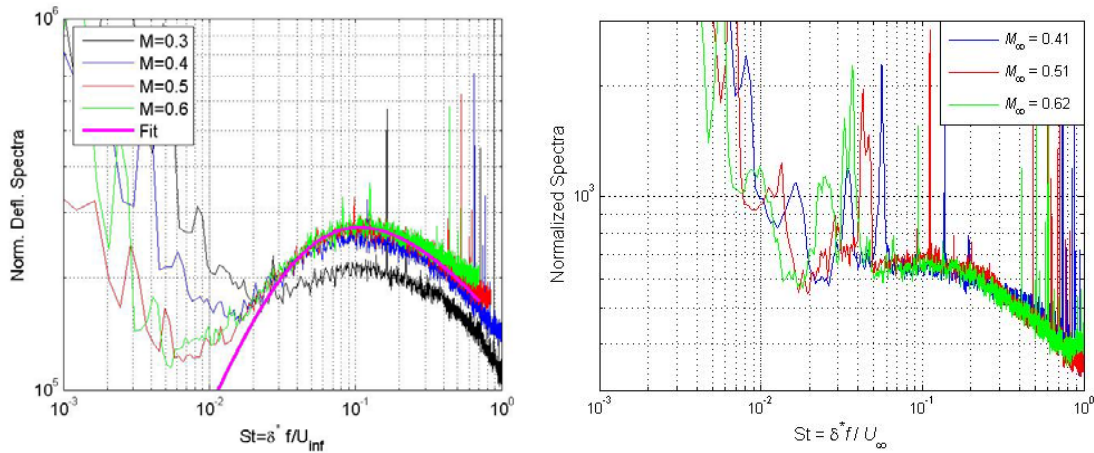

Figure 8: Left: the normalized jitter spectra for the two boundary layer experiment for several Mach numbers. Right: the normalized jitter spectra for the single boundary layer experiment. Large portions of the spectra are corrupted by vibration.

The normalization implies that a 'clean' spectrum, such as the $M_\infty = 0.41$ case of Figure 8, left, can be used to restore OPD_{rms} from a corrupted spectrum, such as those of Figure 7, right as follows:

$$\left\{\frac{OPD_{rms}}{\rho / \rho_{SL} M^2}\right\}_1 = A\left\{\frac{OPD_{rms}}{\rho / \rho_{SL} M^2}\right\}_2, \tag{6}$$

where the index 1 represents the corrupted data, 2 represents the "clean" data and A is a constant obtained by matching the uncorrupted portions of the two normalized spectra so that

$$\left\{\hat{\theta}_{norm}(f\delta^* / U_\infty)\right\}_1 = A\left\{\hat{\theta}_{norm}(f\delta^* / U_\infty)\right\}_2. \tag{7}$$

Figure 9 shows the normalized spectrum matching applied to the single boundary layer data at $M_\infty = 0.41$, 0.51 and 0.62. The reference, or 'clean', case in Figure 8 is the $M_\infty = 0.41$ case from the two boundary layer experiment. The normalized spectra match quite well at high frequencies, St > 0.06, but the spectra for the single boundary layer are corrupted at low frequencies, St < 0.06.
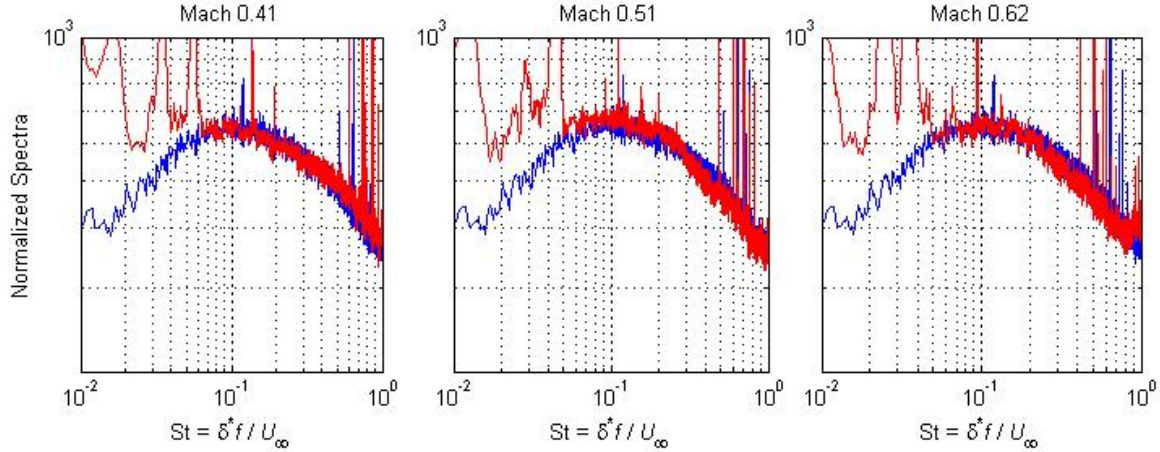
Figure 9: The uncorrupted portions of the normalized spectra are matched as closely as possible by varying the constant *A* in Equation 7.

The reference values of OPD_{rms} , scaling factors and resulting OPD_{rms} values for the single boundary layer are shown in Table 1.

Table 1: Results from the spectral matching shown in Figure 9.

	Reference ($M_\infty = 0.41$)	$M_\infty = 0.41$	$M_\infty = 0.51$	$M_\infty = 0.62$
U_∞ (m/s)	140	140	172	205
ρ / ρ_{SL}	0.87	0.87	0.84	0.79
A	N / A	0.97	0.98	0.98
OPD_{rms} (microns)	0.0069	0.0066	0.001	0.014

Figure 7 shows the OPD_{rms} values for the single boundary layer obtained using the spectral matching plotted against $\delta^*\rho/\rho_{SL}M^2$, along with the data from the double boundary layer experiment. The data show excellent agreement to Equation (3).

Originally, in order to estimate the boundary layer OPD_{rms}, all low frequencies contaminated by mechanical vibrations were removed using a high-pass filter[5]. But the close inspection of spectra for the single and double boundary layer experiments, Figures 5, 6 and 9, have revealed that, although strong, vibration-related peaks are present in the single boundary layer spectra below St < 0.06, which can be easily removed with the high-pass filter, the weak contamination is present up to St = 0.1. This contamination is a probable cause for over-estimating the boundary layer optical distortions, reported earlier[5].

D. Spanwise Correlation Length

The spanwise, or transverse, correlation length was measured in another experiment utilizing the two Malley probe beams in the same streamwise, *x*, location and varied in the spanwise, *z*, direction, see Figure 10. Time series of deflection angles at each location were measured and OPDs were reconstructed using (1). The *OPD* cross correlation coefficients were computed the usual way as

$$\rho_z(\Delta z) = \frac{\overline{OPD(z,t)OPD(z + \Delta z,t)}}{\overline{OPD(z,t)^2}} , \qquad (8)$$

The experimental correlation are shown in Figure 11 along with an exponential curve-fit,

$$\rho_z(\Delta z) = \exp\left(-\frac{|\Delta z|}{\Lambda_z}\right). \tag{9}$$

The exponential fit of the data gives a spanwise correlation length, $\Lambda_z \approx 0.75\,\delta^*$.
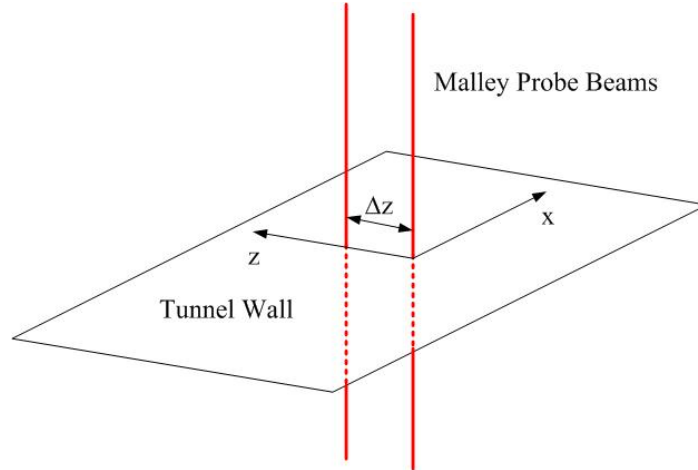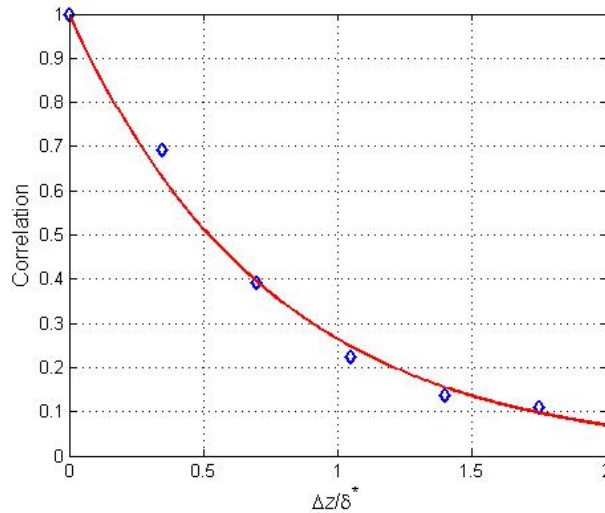

Figure 10. Spanwise correlation set-up.

Figure 11: Optical spanwise correlation decays exponentially with a spanwise separation. The spanwise correlation length, Λ_z, defined by (9), is approximately $0.75\,\delta^*$.

E. Streamwise Correlation Function

A time-delayed auto-correlation function, $R_{OPD}(\tau)$ is defined as,

$$R_{OPD}(\tau) = \overline{OPD(t)OPD(t+\tau)}, \tag{10}$$

where the overbar denotes the temporal averaging. The auto-correlation function can be calculated from the spectral auto-correlation function, $S_{OPD}(f)$,

$$R_{OPD}(\tau) = \int S_{OPD}(f)\exp(2\pi i f\tau)df = \int \frac{\left\langle A_{OPD}(f)A^*_{OPD}(f)\right\rangle}{T}\exp(2\pi i f\tau)df \ , \tag{11}$$

where $A_{OPD}(f)$ is the Fourier transform of OPD(t), T is the block duration, brackets denote an ensemble averaging and the asterisk denotes a complex conjugate. $A_{OPD}(f)$ can be found from the deflection angle spectrum, since from (1) it follows that $A_{OPD}(f) = -\dfrac{\hat{\theta}(f)}{f}$.

In order to compute the auto-correlation function, the normalized deflection angle spectrum, Figure 8, left, was approximated with an empirical curve fit,

$$\left|\hat{\theta}_{norm}(St)\right| \sim \frac{St}{1+(St/0.05)^{4/3}} \ , \tag{12}$$

which is shown as a magenta line in Figure 8, left. Using this empirical deflection angle spectrum, the normalized auto-correlation function $\rho_x(\tau) = R_{OPD}(\tau)/R_{OPD}(0)$ can be calculated using (11) and, using the frozen convection assumption, the time delay was converted into the streamwise separation, $\Delta x = -U_c\,\tau$. The result is plotted in Figure 12. Compared with the spanwise correlation function, Figure 10, the streamwise correlations decay slower. The integral streamwise length, computed as $\Lambda_x = \int \rho_x(\Delta x)d\Delta x$, was found to be $\Lambda_x = 5.2\delta^*$. This length correlates well with optical correlation length of $4\delta^*$, reported in [3]. All these findings indicate the presence of large-scale streamwise-elongated optically-aberrating structures in the outer part of the boundary layer, convecting at approximately 0.87 of the freestream velocity.

Finally, it is worth mentioning that the previous studies[7] have found the streamwise correlation length to be $2\delta^*$. They used the high-pass filter technique which, as it was discussed earlier, removes all low frequencies, including frequencies related to the boundary layer dynamics. Therefore, this high-pass filter technique underestimates the effect from large-scale harmonics and underpredicts the streamwise length.
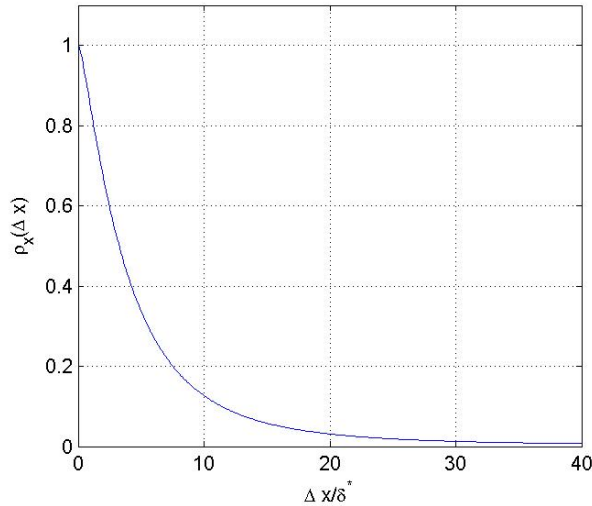

Figure 12. The boundary layer streamwise auto-correlation function.

IV.   Boundary Layer Wavefront Simulations.

Knowing the streamwise and spanwise spectral functions, one can construct uncorrelated series of 2-D boundary layer wavefronts, $W(x,z)$, which, on average, satisfy the observed boundary layer statistics, that is,

$$\overline{W(x,z)W(x+\Delta x, z)} = \rho(\Delta x),$$

$$\overline{W(x,z)W(x, z+\Delta z)} = \rho(\Delta z) \tag{13}$$

$$W_{rms} \equiv OPD_{rms} = 1.6 \times 10^{-5} \frac{\rho}{\rho_{SL}} \delta^* M^2$$

Without loss of generality, we will construct wavefronts which have a normalized deviation, $W_{rms} = 1$.

We construct wavefronts as a collection of uncorrelated 2-D harmonics with random phases,

$$W_n(x,z) = \frac{\int\limits_{-\infty}^{\infty}\int\limits_{-\infty}^{\infty} \sqrt{\lambda(k_x, k_z)}\sqrt{\frac{a_n^2 + b_n^2}{2}} \exp\left(i\{k_x x + k_z z + \phi_n\}\right)dk_x dk_z}{\sqrt{\int\limits_{-\infty}^{\infty}\int\limits_{-\infty}^{\infty} \lambda(k_x, k_z)dk_x dk_z}},$$

where a_n and b_n are random, normally distributed coefficients with a zero mean and a unity standard deviation, a_n , $b_n \sim N(0,1)$, ϕ_n is a uniformly distributed random phase and $\lambda(k_x,k_z)$ is a spectral energy of each harmonic. Further, we approximate the spectral energy as a product of streamwise and spanwise components, $\lambda(k_x,k_z) = \lambda_x(k_x)\lambda_z(k_z)$, where $\lambda_z(k_z) = \left|\int\limits_{-\infty}^{\infty} \rho_z(\Delta z)\exp(-ik_x\Delta z)d\Delta z\right| = \frac{2\Lambda_z}{1+(\Lambda_z k_z)^2}$ and $\lambda_x(k_x) = |A_{OPD}(k_x)|^2$ can be found from the deflection angle spectrum curve fit (12), using the frozen field assumption, $k_x = \frac{2\pi f}{U_c} = \frac{2\pi f \delta^*}{0.87\delta^* U_\infty} = 2\pi\frac{St}{0.87\delta^*} = \frac{1}{0.138}\frac{St}{\delta^*}$,

$$\lambda_x(k_x) = |A_{OPD}(k_x)|^2 \sim \frac{|\hat{\theta}_{norm}(k_x)|^2}{k_x^2} \sim \frac{1}{\left\{1 + \left(\frac{0.138 k_x \delta^*}{0.05}\right)^{4/3}\right\}^2}$$

Two examples of wavefront realizations as colored surfaces are shown in Figure 13, top plots. As expected, they show the presence of large-scale, streamwise-elongated structures. For comparison, experimentally obtained boundary layer wavefronts from the double-boundary-layer experiment are also shown in Figure 13, bottom. They do reveal the presence of streamwise-elongated optical structures.

These simulations provide statistically correct realizations of the turbulent boundary layers and can be used, for instance, to simulate effects from realistic turbulent boundary layers if the boundary layer thickness, the freestream density and the incoming Mach numbers are provided.

Tomkins and Adrian [8], among many other researchers have found elongated low-momentum vortical regions extending into the outer part of the boundary layer with the streamwise length-scales of approximately $5\delta^*$ and spanwise length-scales between 0.5 and 1.3 δ^*. These length-scales agree well with optical correlation lengths, reported above, providing a further evidence that the origin of these optical aberrations are large-scale vortical structures in the outer portion of the boundary layer. Since these structures are vortical in nature, they would create low-pressure wells and consequently density wells and therefore would be optically active.
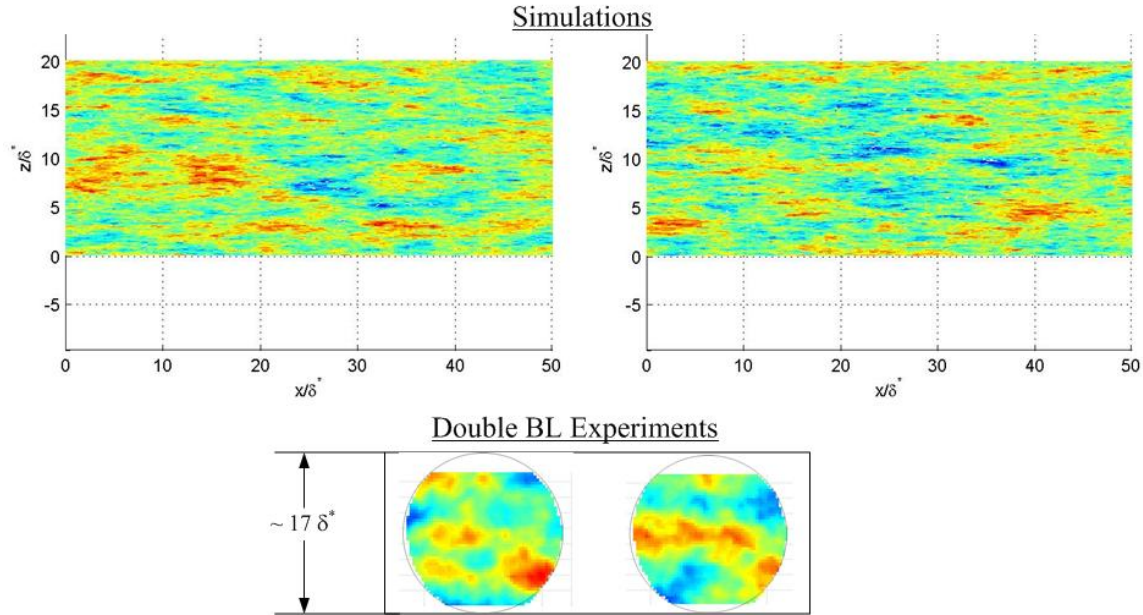
Figure 12. 2-D boundary layer wavefront realizations (top) and experimental wavefronts from double boundary layer (bottom).

V.   Conclusions.

Despite the fact that the aero-optical character of turbulent boundary layers has been studied for decades longer than the better-understood character of separated shear flows, it is far-less understood. As pointed out in this paper, this is due to its lesser optical impact and the fact that this low aberrating influence leads to both instrument signal-to-noise problems and its vulnerability to vibration corruption, a second signal-to-noise-level problem. The results reported here have addressed both of these issues and produced what we believe to be the most-accurate representation of the aero-optical character of turbulent boundary layers to date. While the turbulent boundary layer usually represents a minor reduction in beam quality, there are important applications, such as free-space communication, where its influence may have important system implications. In this regard, we have also presented an approach of using boundary-layer optical statistics to create wavefront realizations useful for system simulations. As importantly, the ability to now measure the optical aberrations provides important insight into the structure of the turbulent boundary layer. Our future efforts in this area will be directed at exploiting this new approach to the study of the structure of turbulence to look more closely at the geometric character of these aberrating structures that are present in the intermittent region of the boundary layer. We also plan to look at transition, which we have previously shown to introduce optical characteristics that do not seem to remain further downstream as the boundary layer becomes more fully developed.

Acknowledgments

References

[1]Tatarskii, V.I. and Zavorotnyi, V.U, "Wave Propagation in Random Media with Fluctuating Turbulent Parameters,", *J. Opt. Soc. Am. A*, Vol. 2, No. 12, pp. 2069-2076.

[2]Jumper, E. J. and Fitzgerald, E. J., "Recent Advances in Aero-Optics," *Progress in Aerospace Sciences*, Vol. 37, 2001, pp. 299-339.

[3]Malley, M., Sutton, G.W., and Kincheloe, N., "Beam-Jitter Measurements for Turbulent Aero-Optical Path Differences, *Applied Optics*, Vol 31, 1992, pp. 4440-4443

[4]S. Gordeyev, T. Hayden and E. Jumper, "Aero-Optical and Flow Measurements Over a Flat-Windowed Turret," *AIAA Journal*, vol. 45, No. 2, pp. 347-357, 2007.

[5]S. Gordeyev, E. Jumper, T. Ng and A. Cain, "Aero-Optical Characteristics of Compressible, Subsonic Turbulent Boundary Layer", 34th AIAA Plasmadynamics and Lasers Conference, Orlando, Florida, 23-26 June, 2003, AIAA Paper 2003-3606.

[6]Nagib, H.M. and Chauhan, K.A., "Scaling of High Reynolds Number Turbulent Boundary Layers Revisited," AIAA Paper 2005-4810, June, 2005.

[7]Buckner, A., Gordeyev, S., and Jumper, E.J., "Optical Aberrations Caused by Transonic Attached Boundary Layers: Underlying Flow Structure," AIAA Paper 2005-0752, Jan. 2005.

[8]Tomkins, C.D. and Adrian, R.J, "Spanwise Structure and Scale Growth in Turbulent Boundary Layers,", *Journal of Fluid Mechanics*, Vol. 490, 2003, pp. 37-74.